Two-photon, fiber-coupled, superresolution microscope for biological imaging

Cite as: APL Photonics **7**, 036102 (2022); https://doi.org/10.1063/5.0075012 Submitted: 12 October 2021 • Accepted: 07 February 2022 • Published Online: 04 March 2022

Brendan M. Heffernan, Peter S. Riley, D Omkar D. Supekar, et al.









ARTICLES YOU MAY BE INTERESTED IN

Non-contact optical magnetic field sensor based on metamaterial nanomechanics APL Photonics **7**, 036101 (2022); https://doi.org/10.1063/5.0081849

Scaling up silicon photonic-based accelerators: Challenges and opportunities APL Photonics 7, 020902 (2022); https://doi.org/10.1063/5.0070992

An ITO-graphene heterojunction integrated absorption modulator on Si-photonics for neuromorphic nonlinear activation

APL Photonics 6, 120801 (2021); https://doi.org/10.1063/5.0062830





Two-photon, fiber-coupled, super-resolution microscope for biological imaging

Cite as: APL Photon. 7, 036102 (2022); doi: 10.1063/5.0075012 Submitted: 12 October 2021 • Accepted: 7 February 2022 • Published Online: 4 March 2022







Brendan M. Heffernan,¹ Peter S. Riley,¹ Omkar D. Supekar,² D Stephanie A. Meyer,³ D Diego Restrepo,⁴ Mark E. Siemens,⁵ Emily A. Gibson,³ and Juliet T. Gopinath^{1,2,a)} D

AFFILIATIONS

- Department of Physics, University of Colorado Boulder, Boulder, Colorado 80309, USA
- ²Department of Electrical, Computer, and Energy Engineering, University of Colorado Boulder, Boulder, Colorado 80309, USA
- Department of Bioengineering, University of Colorado Anschutz Medical Campus, Aurora, Colorado 80045, USA
- ⁴Department of Cell and Developmental Biology, University of Colorado Anschutz Medical Campus, Aurora, Colorado 80045, USA
- Department of Physics and Astronomy, University of Denver, Denver, Colorado 80210, USA

ABSTRACT

Imaging sub-diffraction dynamics of neural nanostructures involved in behaviors such as learning and memory in a freely moving animal is not possible with existing techniques. Here, we present a solution in the form of a two-photon (2P), fiber-coupled, stimulated emission depletion microscope and demonstrate its capabilities by acquiring super-resolution imaging of mammalian cells. A polarization-maintaining fiber is used to transport both the 2P excitation light (915 nm) and the donut-shaped depletion beam (592 nm), which is constructed by adding two temporally incoherent and orthogonally polarized Hermite–Gaussian fiber modes. The fiber output is insensitive to bending or temperature changes and is the first demonstration toward deep tissue super-resolution imaging in awake behaving animals.

© 2022 Author(s). All article content, except where otherwise noted, is licensed under a Creative Commons Attribution (CC BY) license (http://creativecommons.org/licenses/by/4.0/). https://doi.org/10.1063/5.0075012

I. INTRODUCTION

Two-photon (2P) excited fluorescence miniaturized fiber-coupled microscopes offer an unprecedented view into the neural activity of awake behaving animals. ¹⁻⁷ There are two benefits that stem from using a 2P excitation process. The first is that light with longer wavelengths scatter less in tissue and are therefore able to penetrate deeper into the brain. ^{8,9} The second benefit is the inherent optical sectioning that 2P excitation provides, which greatly decreases out-of-focus photobleaching and background fluorescence. ¹⁰ Yet, there are many processes and features of interest that elude study because of the limits on 2P resolution. As a result, the nanoscale structural understanding of behavior is incomplete.

Diffraction-limited imaging of the dynamics of proteins in small neuronal structures is key to understanding their role in normal brain function and neurological disorders. ^{11–13} For instance, morphological changes in dendritic spine structure, such as spine

shrinkage and elimination, have been linked with learning and memory and neurodegenerative disorders, such as Alzheimer's and Huntington's. 12,14,15 Dendritic spines are known to be highly plastic, changing in shape and size dynamically in response to neuronal activity. 14,16-18 Emerging research has made important contributions to understanding the nanoscale dynamics involved in this plasticity. 12,19 For example, a recent study of inhibitory synapses showed the nanoscale architectural dependence between scaffold and GABAergic receptors.²⁰ Similarly important, axon myelination and saltatory conduction through the nodes of Ranvier mediate rapid action potential propagation along neuronal axons relevant to proper signal processing in the brain,¹¹ but the dynamics of myelin and node of Ranvier structure are not fully understood due to their small size. 15,21 Improved nanoscale resolution can answer questions regarding the roles of protein dynamics in neuronal function.¹³ However, sub-diffraction synapses and other small neural structures

a) Author to whom correspondence should be addressed: juliet.gopinath@colorado.edu

have not been studied in awake behaving animals because there is no method that provides high resolution imaging with low weight miniature microscopes suitable for demanding freely moving animal recordings. Here, we present a 2P fiber-coupled stimulated emission depletion (STED) microscope to address this challenge.

Stimulated emission depletion microscopy (STED) is a natural super-resolution choice for this task because of its compatibility with live cell imaging. ^{24,25} Single photon (1P) excitation STED was first demonstrated in the brains of mice *in vivo* in 2012. ²⁶ Since then, *in vivo* mouse brain studies have elucidated the dynamics of postsynaptic membranes of excitatory synapses in the visual cortex ^{27,28} and actin filaments associated with dendritic spine plasticity. ^{29,30} However, to date, all *in vivo* STED studies have been performed on head-fixed, anesthetized mice, which restricts the range of neuroscientific studies that can be performed. ³¹

Besides STED, super-resolution *in vivo* imaging in whole animal models has been demonstrated using structured illumination microscopy in zebrafish³² and mice.^{33,34} Other super-resolution methods include lattice light sheet, localization microscopies, such as photoactivated localization microscopy (PALM)³⁵ or stochastic optical reconstruction micrscopy (STORM),³⁶ and super-resolution radial fluctuations (SRRF);³⁷ however, these methods are difficult or impossible to implement in scattering samples.

A limiting factor of 1P STED is the short excitation wavelength, which scatters significantly in brain tissue and reduces the typical *in vivo* depth of imaging to between 25 and 40 μ m. 28,29,38 In contrast, 2P STED has shown 3D super-resolution at depths of up to 76 μ m *in vivo* in an anesthetized mouse with the use of adaptive optical techniques. Yarious 2P STED microscopes have been developed over the past decade $^{16,40-45}$ and have proven to be exceptional platforms for studying dendritic spines in fixed tissue slices, 46 live cell cultures, 17 and anesthetized, head-restrained animal subjects. 39,47,48 These breakthrough demonstrations motivate the extension of this technology to awake behaving animal studies.

One major challenge of developing a 2P fiber STED microscope is the reliable delivery of the excitation and spatially structured depletion light through the same fiber. In particular, the crucially dark center of the depletion beam must propagate through the fiber without degradation caused by bending or temperature changes. Early work on a 2P fiber STED endoscope used a double clad fiber and adjusted launch conditions of the depletion beam to selectively couple to the LP_{1,1} mode group.⁴⁹ However, this approach is not robust due to the near degeneracy and destructive interference of modes within this mode group, which will result in a changing intensity and polarization profile when perturbed, ultimately degrading the resolution enhancement.⁵⁰ Another possible solution is to use a wavelength selective phase⁵¹ or polarization⁵² plate to structure the depletion beam while leaving the excitation beam unchanged. However, this requires adding heavy glass elements to a miniature, head-mounted microscope, increasing its weight and complexity. To minimize microscope mass, it is ideal to structure the light and then transport it to the subject. One promising approach is to use customized "vortex" or "ring-core" fibers for which circularly polarized beams with orbital angular momentum are the eigenmodes, making it bend-insensitive.5 A 1P fiber STED microscope was recently demonstrated using this fiber,⁵⁴ but the custom and experimental nature of the fiber means it is not commercially available and is currently difficult to attain, motivating the development of more accessible methods.

We recently proposed and demonstrated bend-insensitive through-fiber 1P STED imaging, utilizing two mutually incoherent higher order modes of polarization maintaining fiber (PMF). This method relies on selective coupling to the even and odd orientations of the $LP_{1,1}$ mode using two mutually incoherent sources. In practice, a single depletion laser source can be used, if it is split into two paths with an optical path length difference that exceeds the coherence length of the laser. The linewidth of many commercially available STED lasers is wide enough to easily achieve this delay, resulting in little to no interference and therefore bend-insensitive output.

In this paper, we use two-photon excitation and a MEMS mirror laser scan system to build a 2P fiber STED microscope. We also explore the unique polarization considerations inherent to the design. Our system provides a direct path for a miniaturized, wearable super-resolution microscope capable of imaging depths beyond those achievable with 1P systems. ^{5,58,59} To our knowledge, this work represents the first demonstration of MEMS mirror scanning in a STED system, as well as the first bend-insensitive 2P fiber STED microscope and the first demonstration of a 2P fiber microscope for super-resolution imaging of mammalian cells. We anticipate that this instrument will find use in head-mounted super-resolution microscopy of awake behaving animals.

II. 2P FIBER STED MICROSCOPE DESIGN

A schematic of our system is depicted in Fig. 1. A home-built Ti:sapphire laser mode locked at 915 nm provides 2P excitation light with a nominal repetition rate of 81 MHz. A small fraction of the laser output is incident on a fast photodiode (Thorlabs PDF10A2) that monitors the pulse train and triggers the depletion laser. A subsequent grating pair adds an estimated -35 000 (fs)² of group delay dispersion (GDD) in order to compensate for the dispersion of the PM fiber and other optical elements in the microscope. The grating pair is in a double pass configuration and consists of two gold gratings with a line spacing of 300 grooves per millimeter and a blaze wavelength of 1000 nm (Edmund Optics 49-572). The beam then passes through an optical isolator (EO Technology BB-05-I-000-090) and is directed onto a short-pass dichroic (Chroma zt775sp-2p-uf3) before being coupled into the PM fiber. The polarization maintaining fiber (Thorlabs P1-780PM-FC-1) is 1 m long and has a core diameter of 4.5 μ m, making it single mode at 915 nm while possessing three modes at 592 nm (neglecting polarization). We attain maximally compressed pulses with a duration of ≈140 fs at the output of the PMF, as measured by autocorrelation. Average powers at the back aperture of the objective are between 15 and 20 mW, corresponding to 600-800 W peak powers on sample, assuming optimal pulse compression.

The depletion laser is a Katana HP-06 (NKT Photonics) that outputs ~500 ps pulses of 592 nm light. The beam from this laser is passed through a 3× telescope and is incident on a spatial light modulator (SLM) (Meadowlark P1920-0405-0785-HDMI). A half wave plate (HWP) is used to align the polarization to the preferred axis of the SLM for maximum efficiency. A blazed diffraction grating with a π phase step in the middle is displayed on the SLM in order to shape the beam to match the higher order mode of the PM fiber.

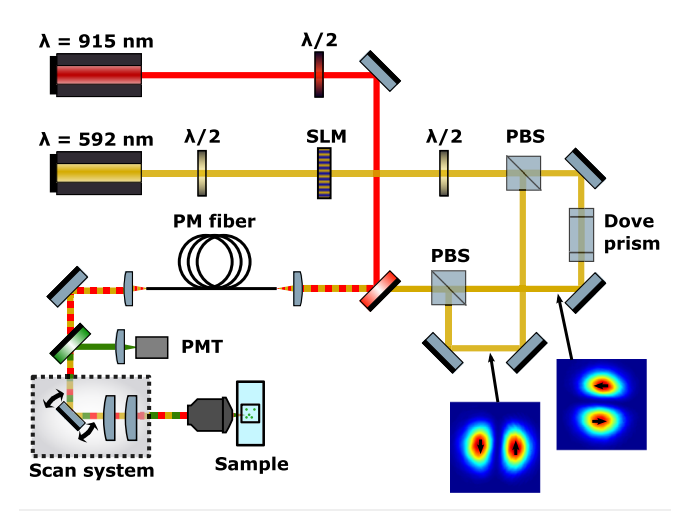


FIG. 1. A diagram of the 2P fiber STED microscope. SLM: spatial light modulator, PBS: polarizing beam splitter, PM fiber: polarization maintaining fiber, and PMT: photomultiplier tube. Insets in the lower right corner show the beam shape and instantaneous polarization (black arrows) of the two higher order modes of the PM fiber used to construct a donut beam. Light from the depletion laser is incident on a half wave plate (HWP) to rotate the polarization to the preferred axis of the SLM. The beam is then shaped using an SLM in order to couple efficiently to the higher order modes of PMF. A PBS splits the shaped beam into two arms of a Mach-Zehnder interferometer. In one arm, a dove prism rotates the intensity profile by 90° to couple to the orthogonally oriented mode in PMF. It also adds a 74 ps delay, much greater than the 6.5 ps coherence time of the source. The two arms of the interferometer are recombined at a PBS and traverse a highpass dichroic before coupling into fiber. The excitation laser passes through an isolator and quarter wave plate before being coupled into the same PMF. The fiber output is collimated and traverses the low-pass detection dichroic before entering the MEMS mirror scan system. Fluorescence from the sample is collected and descanned before the detection dichroic directs it onto a PMT.

The polarization of the beam is then rotated to 45° and split into two paths using a polarizing cube beam splitter (PBS). In one path, a dove prism is used to rotate the intensity profile of the beam by 90° so that the sum of the two modes forms the donut-shaped depletion beam (see the inset in Fig. 1). The dove prism also adds a path length difference greater than the coherence length of the Katana, resulting in minimal interference between the two modes creating the donut depletion beam. There is still significant temporal overlap between the two modes, and STED efficiency is not affected. The two paths are rejoined using another PBS, and the beam is coupled to the higher order modes of the PM fiber. The fiber output is collimated using a 20× apochromatic objective (Mitutoyo MY20X-824) and aligned into the scan system.

As the driver of our scan system, we choose to use a MEMS mirror (with a diameter of 3.6 mm) (Mirrorcle Tech A7B2.1-3600AL-TINY20.4-A/TP) for two primary reasons. First, the MEMS mirror is readily integrated into miniaturized head-mounted microscopes. 5.58,59 Second, the MEMS mirror can actuate two axes at a single plane. This simplifies the optical arrangement compared to typical telecentric galvo systems used for STED, for which a relay lens is needed to image the first mirror onto the second. 16,47 The controller for the mirror [Mirrorcle Tech universal serial bus (USB)-SL MZ] has an onboard programmable frequency filter that removes the resonant frequency of the MEMS mirror from the control

voltage, allowing the mirror to actuate without ringing. Typical imaging parameters result in a pixel dwell time of $50 \mu s$.

Commercially available scan (Thorlabs SL50-CLS2) and tube (Thorlabs TTL200MP) lenses are used, resulting in 4× magnification of the beams entering the final objective: a 1.4 NA oil immersion objective (Olympus UPLSAPO 100XO). The objective to sample spacing can be coarse adjusted using a motorized mount (Thorlabs ZMF2020), and fine adjustment is made using a piezo-actuated mount (Mad City Labs C-focus system). The stage features a closed-loop feedback to maintain focus at a set position.

Fluorescence collected by the objective is descanned through the system before being split from the beam path using a low-pass dichroic (Chroma t560lpxxt-uf). The fluorescence is focused onto a PMT using a 200 mm focal length lens. The voltage signal from the PMT (Hamamatsu H7422P-40) is fed into a signal conditioning box (Hamamatsu C9744) that converts the continuous voltage into discrete transistor-transistor logic (TTL) pulses that are counted using a data acquisition card (DAQ) card (NI PCIe-6353).

Power throughput of the depletion laser from the laser source to microscope scan system is currently estimated to be 5%-10% but is not optimized and is limited by the chromatic aberration of our fiber coupling lens and our choice of SLM.

III. IMAGING RESULTS

A. Characterizing system resolution

The resolution of a STED system can change from sample to sample due to the properties of the fluorophores and the conditions to which they are subjected. Even for a given sample, different metrics of resolution can be used: full width half maximum (FWHM) of a Gaussian or Lorentzian fit, Rayleigh criterion, or Fourier domain analysis. Here, we fit an ensemble of beads to Gaussian or Lorentzian functions and extract a distribution of FWHM values as a measure of the transverse resolution. This method provides a robust statistical estimate of the resolution that protects against the influence of intrinsic Poissonian noise that can result in over or underestimate of a single measurement. This method has been shown to give similar results as the Fourier domain technique of Fourier ring correlation (FRC).

The FWHM values for an image are extracted using code written in MATLAB. Bead locations are found using a peak finding algorithm. A region of interest (ROI) is selected around each bead, and the results are verified by the user. The peaks that are too near each other are eliminated in order to fit only single, isolated beads. Each region of interest is then fit to a two-dimensional function using a least-squares method: for standard 2P images, a Gaussian is used, and for STED images, a Lorentzian is used. The form of the 2D Lorentzian is

$$A\frac{\Gamma_{x} \Gamma_{y}}{4} \left(\frac{\Gamma_{x}/2}{(x-x_{0})^{2} + (\Gamma_{x}/2)^{2}} \right) \left(\frac{\Gamma_{y}/2}{(y-y_{0})^{2} + (\Gamma_{y}/2)^{2}} \right) + B, \quad (1)$$

where A is the number of counts at the center, $\Gamma_{x,y}$ is the FWHM of the function along x or y, x_0, y_0 are the centers of the Lorentzian in x and y directions, and B is a background term. For each fit, the coefficient of determination (r^2) is calculated, and the code iterates over the ROI size in order to maximize the sum of r^2 values. This typically results in ROI sizes of $580 \times 580 \text{ nm}^2$ for

diffraction-limited images and 320×320 nm² for STED. For STED images presented here, Lorentzian fits produce a marginally larger sum of r^2 values compared to Gaussian fitting, indicating that a Lorentzian function more adequately describes the STED image of a bead. This is consistent with calculations examining a projected 2D image while considering the effective STED illumination volume convolved with a three-dimensional sample structure, such as microtubules. FWHM values from a Lorentzian fit are slightly smaller than for a Gaussian, though in many cases they are within 10 nm of each other.

The images of 100 nm fluorescent beads (Thermo Fisher Scientific F8803) are shown in Fig. 2 with (b) and without (a) the use of depletion light. The sample was prepared such that the fluorescent beads are confined to the cover slip surface. The measured full width half maximum (FWHM) value for multiple beads was extracted using the process outlined above, and their distributions are shown in Fig. 2(c). The average values of the distributions are 296 ± 12 nm without STED and 139 ± 18 nm with STED, where the uncertainty given is the standard deviation of the distribution. This demonstrates a two-fold improvement of resolution.

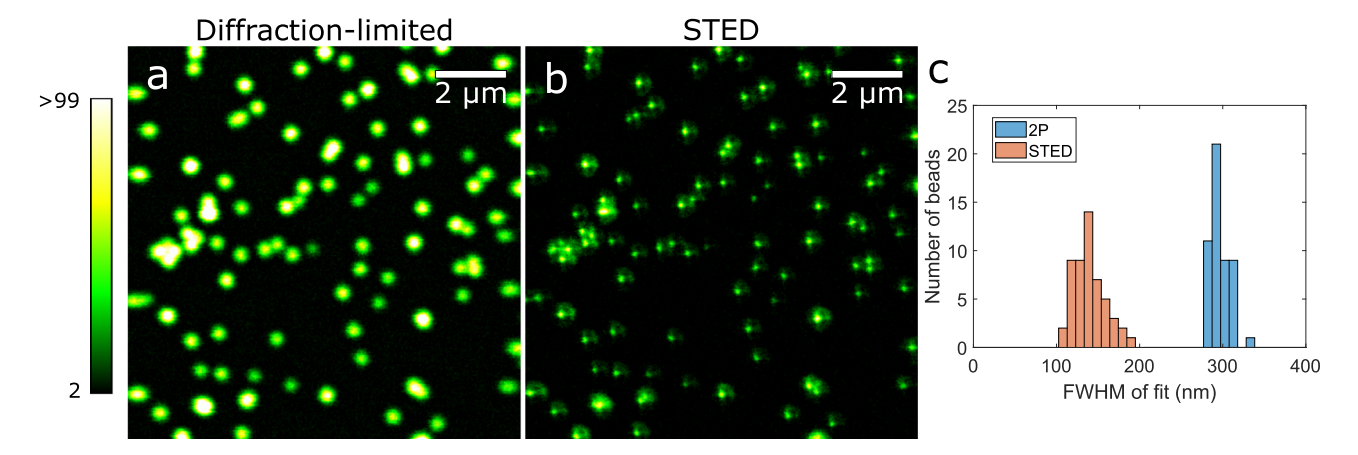


FIG. 2. Images of 100 nm fluorescent beads (a) without the use of STED and (b) with the use of STED. Each image is 512×512 pixels. Approximately 36 mW of STED power and 16 mW of excitation power was used, measured at the back aperture of the objective. The pixel size is 22 nm, and the acquisition time was $50 \,\mu s$ at each pixel. A Gaussian blur filter (waist of 0.7 pixels) was applied to reduce noise, and the background has been subtracted in that order. (c) Histogram of FWHM values extracted from raw bead images. For the non-STED images, a 2D Gaussian fit was used, whereas for the STED images, a Lorentzian was used. The fits with $r^2 < 0.6$ were not used, as well as fit FWHM values that were greater two standard deviations above or below the median. The non-STED distribution has an average of 296 ± 12 nm, while the STED distribution has an average of 139 ± 18 nm, where the uncertainty given is one standard deviation. This shows a two-fold enhancement in resolution for this sample.

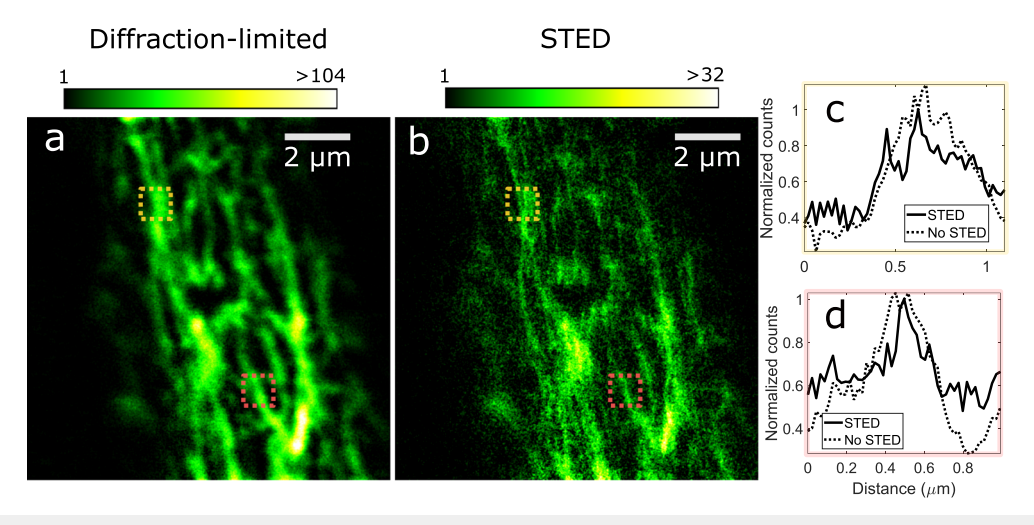


FIG. 3. Images of cells immunostained for vimentin using Abberior star green (Abberior IG-4011). The images in (a) and (b) are 512×512 pixels with a pixel size of 22 nm and a dwell time of $50 \mu s$. They were acquired using 19 mW of excitation and 34 mW of depletion power, measured at the back aperture of the objective. The scale bars are $2 \mu m$. For visual clarity, the 2P image in (a) and STED image in (b) have had a Gaussian blur filter with a waist of 0.7 pixels (15 nm) applied, and the background was subtracted using a rolling ball with radius of 50 pixels in ImageJ. For the STED image, the background caused by the depletion light was subtracted off prior to the processing listed above. Normalized linecuts of raw data from two regions of interest comparing (a) and (b) are shown in (c) and (d). Linecuts were taken from raw data along the x direction and were averaged with five neighboring pixels along y in order to reduce noise.

The measured axial resolution of our system in both standard 2P and 2P STED modalities is 690 nm, in agreement with theoretical calculations of 685 nm (see the supplementary material). 66,67 This value does not change for STED modality because we currently do not have any added axial confinement of the excitation volume, as could be achieved through the use of, for instance, "bottle beams." 68–70

B. Imaging mammalian cells

We also acquired images of mammalian cells immunostained for vimentin with Abberior star green (Abberior IG-4011), as shown in Fig. 3. A clear improvement in resolution can be seen by comparing Figs. 3(a) and 3(b), and quantitative evidence of resolution improvement is given by taking linecuts across the raw image data, as shown in Figs. 3(c) and 3(d). Additional images, as well

as a comparison of raw and processed data, are provided in the supplementary material.

IV. POLARIZATION CONSIDERATIONS

We have presented a novel 2P fiber STED microscope and demonstrated its ability to achieve resolutions down to 139 nm using fluorescent beads. We have also verified its ability to achieve super-resolution in biologically relevant samples. However, due to the unique design, several aspects of this microscope warrant further discussion, specifically how image formation is affected by the polarization of the STED and excitation beams.

Tight-focusing calculations based on the Deybe–Wolf integral⁷¹ show that the two fiber modes making up our donut must be linearly polarized in the direction of their respective null [see Fig. 1, as well as Figs. 4(a) and 4(d)]. If the beam was not polarized in this

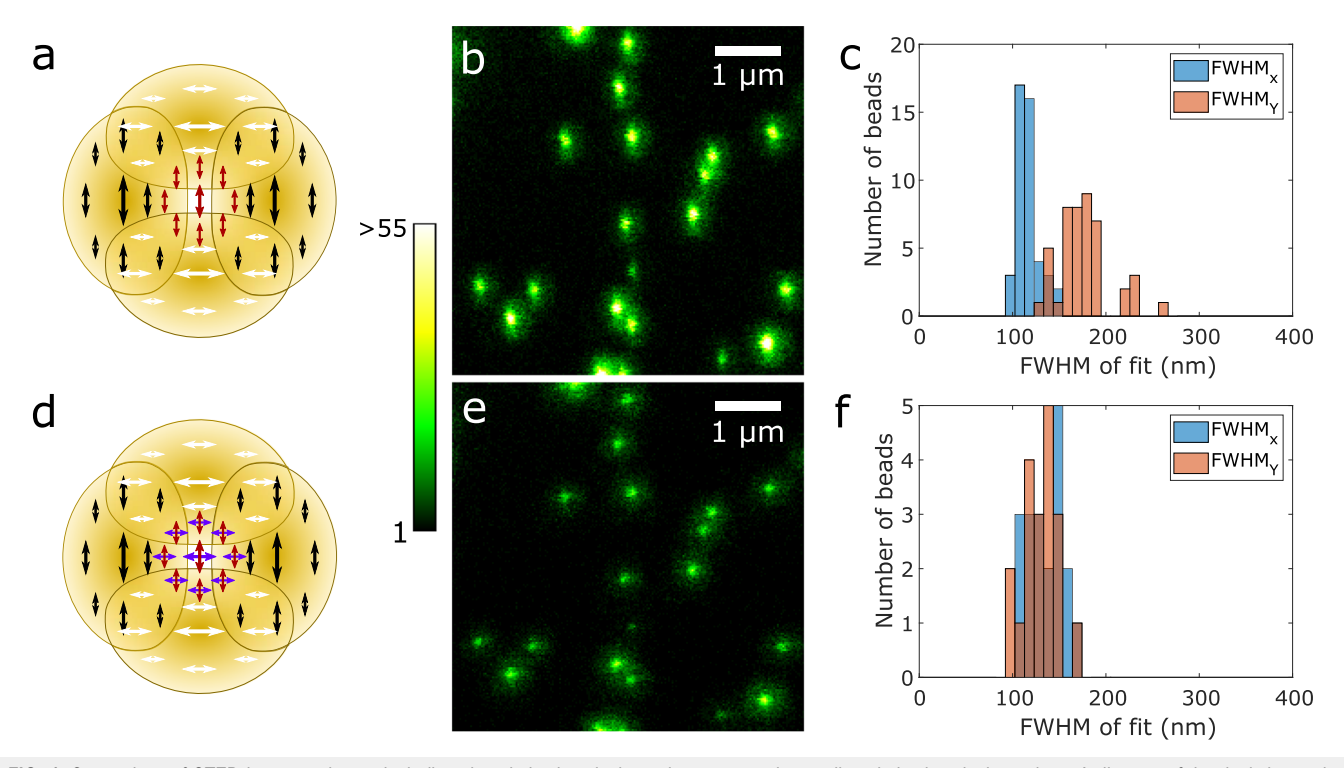


FIG. 4. Comparison of STED images using a single linearly polarized excitation pulse vs two orthogonally polarized excitation pulses. A diagram of the depletion and excitation light polarization is presented in (a). Black and white arrows indicate the depletion beam polarizations, which do not interfere due to lack of temporal coherence. Red arrows show the polarization of the excitation pulse. A portion of the resulting image of 100 nm fluorescent beads is shown in (b). Distributions of measured FWHM values along the x and y directions for the full image are plotted in (c). There is a clear difference in resolution along the two axes due to less efficient fluorescence depletion along the y axis. A pictorial representation of using two orthogonally polarized excitation pulses is shown in (d). Purple arrows denote the polarization of a second excitation pulse, and the excitation polarizations do not interfere because they are temporally separated by 1.6 ps. A portion of the resulting image is shown in (e), and the FWHM values along x and y are again plotted in (f). The color scale for both images in (b) and (e) is the same, as is the total excitation power used. Images have been averaged over two acquisitions to reduce noise and have a pixel size of 27.6 nm. The full images are 400 by 400 pixels; (b) and (e) show a 193 \times 192 pixels subset of the full images. The dwell time was 50 μ s. In the case of a single pulse polarized along y, the average FWHM along x is 116 \pm 12 nm and along y is 176 \pm 28 nm. For two temporally separated, orthogonally polarized excitation pulses, the average resolution along x is found to be 136 \pm 19 nm and along y it is 130 \pm 18 nm. This demonstrates that while images using two excitation pulses are more symmetric, they have fewer counts. It also reveals that using a single linearly polarized excitation pulses, assuming the same total average power.

manner, it would develop a relatively strong component of polarization along the direction of propagation, effectively "filling in" the dark center of the beam and resulting in low signal to noise and degraded resolution. This constraint is the reason that traditional 2D STED setups using light with orbital angular momentum (OAM) for the depletion donut must use circularly polarized light.^{72–74}

The linear polarization of the depletion beam affects image formation. In the case of rigidly bound fluorophores with randomly oriented dipoles that are all efficiently excited, our depletion beam will not quench fluorescence as effectively along the x and y directions because our donut beam will be exclusively polarized in a single direction here. ^{52,75} This is because the polarization will be orthogonal to the dipole orientation of some subset of fluorophores. This will result in a "pedestal" along the x and y directions of the point-spread function (PSF), as can be faintly seen in Fig. 2(b) and also shown along the y direction in Fig. 4(b). As noted in previous works, this feature can also be used to determine the orientation of a dipole and could perhaps be used to extract information about the rotational freedom of the fluorophore. ^{52,75}

The polarization of the excitation light is also of interest. Ideally, pulses in our system would be circularly polarized to uniformly excite all dipole orientations efficiently. However, the PM fiber used for bend-insensitive transmission has linearly polarized eigenmodes. As an alternative, the light from our Ti:sapphire laser is polarized linearly at 45° with respect to the slow axis of the PM fiber. At the fiber output, this results in two ≈ 140 fs pulses that are orthogonally polarized and delayed by ≈ 1.6 ps, measured via autocorrelation. Compared to linear polarization along the fast or slow axis, this orientation yields a more symmetric STED PSF, as shown in Figs. 4(c) and 4(f). However, it also decreases fluorescent counts, given the same average power and results in degraded resolution along one direction compared to the linearly polarized excitation case, as shown in Figs. 4(b) and 4(e).

Our method of generating a donut depletion using incoherent addition of PM fiber eigenmodes results in bend-insensitive imaging, as demonstrated in Ref. 55. The polarization of the excitation pulses is consistent and unaffected by bending due to the large birefringence of the fiber.

Future work involving this platform could take several directions. Perhaps the most immediate is translating this powerful technique to *in vivo* applications, which will involve engineering a suitable head-mounted microscope. The imaging depth and resilience to aberration of our approach should also be studied and compared to a more traditional optical vortex beam.

V. CONCLUSIONS

We have demonstrated super-resolution imaging in mammalian cells using a 2P fiber-coupled STED microscope. Images of both fluorescent beads and mammalian cells were acquired using 2P and STED modalities, and at least a two-fold enhancement in resolution was found. This is the first bend tolerant 2P fiber STED microscope and the first STED microscope to utilize a MEMS mirror scanner. In addition, this design provides intrinsic transverse overlap of excitation and depletion beams, simplifying the typical STED microscope alignment. It is also easily adapted to different excitations and STED wavelengths and can even be extended to multicolor imaging. This flexible platform provides a direct route to

super-resolution imaging at deeper tissue depths in an awake behaving animal than would be possible using one-photon excitation due to the increased penetration depth of the 2P excitation light.

SUPPLEMENTARY MATERIAL

See supplementary material for characterization of the microscope PSF and additional STED images of mammalian cells.

ACKNOWLEDGMENTS

We would like to thank Karsten Bahlmann at Abberior GmbH for providing cell samples. We also thank Rytis Prekeris and Arianna Gentile Polese for providing stained HeLa cells. We acknowledge Adi Natan for the peak-finding code used to extract imaged bead FWHM values and thank Christian Gentry for his help building the Ti:sapphire laser. This work was supported by the National Science Foundation (NSF) (Grant Nos. DMR 1553905, ECCS 1509733, ECCS 1509928, ECCS 1554704, DBI 1337573, and DBI 1919541) and the University of Colorado Boulder Imaging Science IRT Seed Grant. Publication of this article was funded by the University of Colorado Boulder Libraries Open Access Fund.

AUTHOR DECLARATIONS

Conflict of Interest

The authors declare no conflicts of interest.

DATA AVAILABILITY

The data that support the findings of this study are openly available in CU neurophotonics GitHub at https://github.com/CUNeurophotonics.

REFERENCES

- ¹F. Helmchen, M. S. Fee, D. W. Tank, and W. Denk, "A miniature head-mounted two-photon microscope," Neuron 31, 903–912 (2001).
- ²B. A. Flusberg, A. Nimmerjahn, E. D. Cocker, E. A. Mukamel, R. P. J. Barretto, T. H. Ko, L. D. Burns, J. C. Jung, and M. J. Schnitzer, "High-speed, miniaturized fluorescence microscopy in freely moving mice," Nat. Methods 5, 935–938 (2008).
 ³J. Sawinski, D. J. Wallace, D. S. Greenberg, S. Grossmann, W. Denk, and J. N. D. Kerr, "Visually evoked activity in cortical cells imaged in freely moving animals," Proc. Natl. Acad. Sci. U. S. A. 106, 19557–19562 (2009).
- ⁴F. Helmchen, W. Denk, and J. N. Kerr, "Miniaturization of two-photon microscopy for imaging in freely moving animals," Cold Spring Harbor Protoc. **2013**, 904.
- ⁵W. Zong, R. Wu, M. Li, Y. Hu, Y. Li, J. Li, H. Rong, H. Wu, Y. Xu, Y. Lu, H. Jia, M. Fan, Z. Zhou, Y. Zhang, A. Wang, L. Chen, and H. Cheng, "Fast high-resolution miniature two-photon microscopy for brain imaging in freely behaving mice," Nat. Methods 14, 713–719 (2017).
- ⁶B. N. Ozbay, G. L. Futia, M. Ma, V. M. Bright, J. T. Gopinath, E. G. Hughes, D. Restrepo, and E. A. Gibson, "Three dimensional two-photon brain imaging in freely moving mice using a miniature fiber coupled microscope with active axial-scanning," Sci. Rep. 8, 8108 (2018).
- ⁷W. Zong, R. Wu, S. Chen, J. Wu, H. Wang, Z. Zhao, G. Chen, R. Tu, D. Wu, Y. Hu, Y. Xu, Y. Wang, Z. Duan, H. Wu, Y. Zhang, J. Zhang, A. Wang, L. Chen, and H. Cheng, "Miniature two-photon microscopy for enlarged field-of-view, multiplane and long-term brain imaging," Nat. Methods 18, 46–49 (2021).
- ⁸W. Denk, J. H. Strickler, and W. W. Webb, "Two-photon laser scanning fluorescence microscopy," Science **248**, 73–76 (1990).

ARTICLE APL Photonics scitation.org/journal/app

- ⁹V. E. Centonze and J. G. White, "Multiphoton excitation provides optical sections from deeper within scattering specimens than confocal imaging," Biophys. J. 75, 2015-2024 (1998).
- $^{10}\mathrm{K}.$ Svoboda and R. Yasuda, "Principles of two-photon excitation microscopy and its applications to neuroscience," Neuron 50, 823-839 (2006).
- ¹¹R. D. Fields, "A new mechanism of nervous system plasticity: Activitydependent myelination," Nat. Rev. Neurosci. 16, 756-767 (2015).
- ¹²K. Runge, C. Cardoso, and A. de Chevigny, "Dendritic spine plasticity: Function and mechanisms," Front. Synaptic Neurosci. 12, 36 (2020).
- ¹³Y. Wang, J. Lin, Q. Zhang, X. Chen, H. Luan, and M. Gu, "Fluorescence nanoscopy in neuroscience," Engineering (in press) (2021).
- ¹⁴E. Pchitskaya and I. Bezprozvanny, "Dendritic spines shape analysis— Classification or clusterization? Perspective," Front. Synaptic Neurosci. 12, 31
- 15 E. R. Kandel, J. H. Schwartz, A. J. Hudspeth, S. A. Siegelbaum, and T. M. Jessell, Principles of Neural Science (McGraw-Hill Medical, New York; Toronto, ON,
- 16 P. Bethge, R. Chéreau, E. Avignone, G. Marsicano, and U. V. Nägerl, "Twophoton excitation STED microscopy in two colors in acute brain slices," Biophys. [. 104, 778-785 (2013).
- ¹⁷J. Tønnesen, G. Katona, B. Rózsa, and U. V. Nägerl, "Spine neck plasticity regulates compartmentalization of synapses," Nat. Neurosci. 17, 678-685 (2014).
- ¹⁸J. Tønnesen and U. V. Nägerl, "Dendritic spines as tunable regulators of synaptic signals," Front. Psychiatry 7, 101 (2016).
- ¹⁹ A. S. Vallés and F. J. Barrantes, "Nanoscale sub-compartmentalization of the dendritic spine compartment," Biomolecules 11, 1697 (2021).
- ²⁰K. C. Crosby, S. E. Gookin, J. D. Garcia, K. M. Hahm, M. L. Dell'Acqua, and K. R. Smith, "Nanoscale subsynaptic domains underlie the organization of the inhibitory synapse," Cell Rep. 26, 3284-3297 (2019).
- ²¹E. D'Este, D. Kamin, F. Balzarotti, and S. W. Hell, "Ultrastructural anatomy of nodes of Ranvier in the peripheral nervous system as revealed by STED microscopy," Proc. Natl. Acad. Sci. U. S. A. 114, E191-E199 (2017).
- ²²D. Fitzner, A. Schneider, A. Kippert, W. Möbius, K. I. Willig, S. W. Hell, G. Bunt, K. Gaus, and M. Simons, "Myelin basic protein-dependent plasma membrane reorganization in the formation of myelin," EMBO J. 25, 5037-5048 (2006).
- ²³O. Steshenko, D. M. Andrade, A. Honigmann, V. Mueller, F. Schneider, E. Sezgin, S. W. Hell, M. Simons, and C. Eggeling, "Reorganization of lipid diffusion by myelin basic protein as revealed by STED nanoscopy," Biophys. J. 110, 2441–2450
- ²⁴V. Westphal, S. O. Rizzoli, M. A. Lauterbach, D. Kamin, R. Jahn, and S. W. Hell, "Video-rate far-field optical nanoscopy dissects synaptic vesicle movement," cience 320, 246-249 (2008).
- ²⁵B. Hein, K. I. Willig, and S. W. Hell, "Stimulated emission depletion (STED) nanoscopy of a fluorescent protein-labeled organelle inside a living cell," Proc. Natl. Acad. Sci. U. S. A. 105, 14271-14276 (2008).
- ²⁶S. Berning, K. I. Willig, H. Steffens, P. Dibaj, and S. W. Hell, "Nanoscopy in a living mouse brain," Science 335, 551 (2012).
- ²⁷W. Wegner, A. C. Mott, S. G. N. Grant, H. Steffens, and K. I. Willig, "In vivo STED microscopy visualizes PSD95 sub-structures and morphological changes over several hours in the mouse visual cortex," Sci. Rep. 8, 219 (2018).
- ²⁸ J.-M. Masch, H. Steffens, J. Fischer, J. Engelhardt, J. Hubrich, J. Keller-Findeisen, E. D'Este, N. T. Urban, S. G. N. Grant, S. J. Sahl, D. Kamin, and S. W. Hell, "Robust nanoscopy of a synaptic protein in living mice by organic-fluorophore labeling," Proc. Natl. Acad. Sci. U. S. A. 115, E8047-E8056
- ²⁹ K. I. Willig, H. Steffens, C. Gregor, A. Herholt, M. J. Rossner, and S. W. Hell, "Nanoscopy of filamentous actin in cortical dendrites of a living mouse," Biophys. J. 106, L01-L03 (2014).
- ³⁰W. Wegner, P. Ilgen, C. Gregor, J. van Dort, A. C. Mott, H. Steffens, and K. I. Willig, "In vivo mouse and live cell STED microscopy of neuronal actin plasticity using far-red emitting fluorescent proteins," Sci. Rep. 7, 11781 (2017).
- ³¹ H. Steffens, W. Wegner, and K. I. Willig, "*In vivo* STED microscopy: A roadmap to nanoscale imaging in the living mouse," Methods **174**, 42–48 (2020).
- ³² A. G. York, S. H. Parekh, D. D. Nogare, R. S. Fischer, K. Temprine, M. Mione, A. B. Chitnis, C. A. Combs, and H. Shroff, "Resolution doubling in live, multicellular

- organisms via multifocal structured illumination microscopy," Nat. Methods 9, 749-754 (2012).
- 33 R. Turcotte, Y. Liang, M. Tanimoto, Q. Zhang, Z. Li, M. Koyama, E. Betzig, and N. Ji, "Dynamic super-resolution structured illumination imaging in the living brain," Proc. Natl. Acad. Sci. U. S. A. 116, 9586-9591 (2019).
- ³⁴B. E. Urban, L. Xiao, B. Dong, S. Chen, Y. Kozorovitskiy, and H. F. Zhang, "Imaging neuronal structure dynamics using 2-photon super-resolution patterned excitation reconstruction microscopy," J. Biophotonics 11, e201700171 (2018).
- 35 E. Betzig, G. H. Patterson, R. Sougrat, O. W. Lindwasser, S. Olenych, J. S. Bonifacino, M. W. Davidson, J. Lippincott-Schwartz, and H. F. Hess, "Imaging intracellular fluorescent proteins at nanometer resolution," Science 313, 1642
- ³⁶M. J. Rust, M. Bates, and X. Zhuang, "Sub-diffraction-limit imaging by stochastic optical reconstruction microscopy (STORM)," Nat. Methods 3, 793-796 (2006).
- ³⁷N. Gustafsson, S. Culley, G. Ashdown, D. M. Owen, P. M. Pereira, and R. Henriques, "Fast live-cell conventional fluorophore nanoscopy with ImageJ through super-resolution radial fluctuations," Nat. Commun. 7, 12471 (2016).
- ³⁸L. Schermelleh, A. Ferrand, T. Huser, C. Eggeling, M. Sauer, O. Biehlmaier, and G. P. C. Drummen, "Super-resolution microscopy demystified," Nat. Cell Biol. 21, 72-84 (2019).
- ³⁹M. G. M. Velasco, M. Zhang, J. Antonello, P. Yuan, E. S. Allgeyer, D. May, O. M'Saad, P. Kidd, A. E. S. Barentine, V. Greco, J. Grutzendler, M. J. Booth, and J. Bewersdorf, "3D super-resolution deep-tissue imaging in living mice," Optica 8, 442-450 (2021).
- ⁴⁰J. B. Ding, K. T. Takasaki, and B. L. Sabatini, "Supraresolution imaging in brain slices using stimulated-emission depletion two-photon laser scanning microscopy," Neuron 63, 429-437 (2009).
- ⁴¹G. Moneron and S. W. Hell, "Two-photon excitation STED microscopy," Opt. Express 17, 14567 (2009).
- ⁴²Q. Li, S. S. H. Wu, and K. C. Chou, "Subdiffraction-limit two-photon fluorescence microscopy for GFP-tagged cell imaging," Biophys. J. 97, 3224-3228 (2009).
- ⁴³P. Bianchini, B. Harke, S. Galiani, G. Vicidomini, and A. Diaspro, "Singlewavelength two-photon excitation-stimulated emission depletion (SW2PE-STED) superresolution imaging," Proc. Natl. Acad. Sci. U. S. A. 109, 6390-6393
- 44K. T. Takasaki, J. B. Ding, and B. L. Sabatini, "Live-cell superresolution imaging by pulsed STED two-photon excitation microscopy," Biophys. J. 104, 770-777
- ⁴⁵S. Bancelin, L. Mercier, E. Murana, and U. V. Nägerl, "Aberration correction in stimulated emission depletion microscopy to increase imaging depth in living brain tissue," Neurophotonics 8, 035001 (2021).
- ⁴⁶K. Takasaki and B. L. Sabatini, "Super-resolution 2-photon microscopy reveals that the morphology of each dendritic spine correlates with diffusive but not synaptic properties," Front. Neuroanat. 8, 29 (2014).
- ⁴⁷M. J. T. ter Veer, T. Pfeiffer, and U. V. Nägerl, "Two-photon STED microscopy for nanoscale imaging of neural morphology in vivo," Methods Mol. Biol. 1663, 45-64 (2017).
- ⁴⁸T. Pfeiffer, S. Poll, S. Bancelin, J. Angibaud, V. K. Inavalli, K. Keppler, M. Mittag, M. Fuhrmann, and U. V. Nägerl, "Chronic 2P-STED imaging reveals high turnover of dendritic spines in the hippocampus in vivo," eLife 7, e34700 (2018).
- $^{\mathbf{49}}$ M. Gu, H. Kang, and X. Li, "Breaking the diffraction-limited resolution barrier in fiber-optical two-photon fluorescence endoscopy by an azimuthally-polarized beam," Sci. Rep. 4, 3627 (2014).
- ⁵⁰S. Ramachandran and P. Kristensen, "Optical vortices in fiber," Nanophotonics 2, 455-474 (2013).
- $^{\bf 51}{\rm D.}$ Wildanger, J. Bückers, V. Westphal, S. W. Hell, and L. Kastrup, "A STED microscope aligned by design," Opt. Express 17, 16100 (2009).
- 52 M. Reuss, J. Engelhardt, and S. W. Hell, "Birefringent device converts a standard scanning microscope into a STED microscope that also maps molecular orientation," Opt. Express 18, 1049 (2010).
- ⁵³Z. Ma and S. Ramachandran, "Propagation stability in optical fibers: Role of path memory and angular momentum," Nanophotonics 10, 209–224 (2020). ⁵⁴L. Yan, P. Kristensen, and S. Ramachandran, "Vortex fibers for STED
- microscopy," APL Photonics 4, 022903 (2019).

- ⁵⁵B. M. Heffernan, S. A. Meyer, D. Restrepo, M. E. Siemens, E. A. Gibson, and J. T. Gopinath, "A fiber-coupled stimulated emission depletion microscope for bend-insensitive through-fiber imaging," Sci. Rep. **9**, 11137 (2019).
- ⁵⁶J. W. Goodman, Statistical Optics, 2nd ed., Wiley Series in Pure and Applied Optics (John Wiley & Sons, Inc., Hoboken, NJ, 2015).
- ⁵⁷R. D. Niederriter, M. E. Siemens, and J. T. Gopinath, "Simultaneous control of orbital angular momentum and beam profile in two-mode polarization-maintaining fiber," Opt. Lett. **41**, 5736 (2016).
- ⁵⁸ W. Jung, S. Tang, D. T. McCormic, T. Xie, Y.-C. Ahn, J. Su, I. V. Tomov, T. B. Krasieva, B. J. Tromberg, and Z. Chen, "Miniaturized probe based on a microelectromechanical system mirror for multiphoton microscopy," Opt. Lett. 33, 1324 (2008).
- ⁵⁹ W. Piyawattanametha, E. D. Cocker, L. D. Burns, R. P. J. Barretto, J. C. Jung, H. Ra, O. Solgaard, and M. J. Schnitzer, "*In vivo* brain imaging using a portable 2.9 g two-photon microscope based on a microelectromechanical systems scanning mirror," Opt. Lett. 34, 2309 (2009).
- ⁶⁰V. Westphal and S. W. Hell, "Nanoscale resolution in the focal plane of an optical microscope," Phys. Rev. Lett. **94**, 143903 (2005).
- 6¹ J. Demmerle, E. Wegel, L. Schermelleh, and I. M. Dobbie, "Assessing resolution in super-resolution imaging," Methods **88**, 3–10 (2015).
- ⁶² R. P. J. Nieuwenhuizen, K. A. Lidke, M. Bates, D. L. Puig, D. Grünwald, S. Stallinga, and B. Rieger, "Measuring image resolution in optical nanoscopy," Nat. Methods 10, 557–562 (2013).
- ⁶³ N. Banterle, K. H. Bui, E. A. Lemke, and M. Beck, "Fourier ring correlation as a resolution criterion for super-resolution microscopy," J. Struct. Biol. 183, 363–367 (2013).
- ⁶⁴G. Tortarolo, M. Castello, A. Diaspro, S. Koho, and G. Vicidomini, "Evaluating image resolution in stimulated emission depletion microscopy," Optica 5, 32 (2018).

- ⁶⁵ A. E. S. Barentine, L. K. Schroeder, M. Graff, D. Baddeley, and J. Bewersdorf, "Simultaneously measuring image features and resolution in live-cell STED images," Biophys. J. **115**, 951–956 (2018).
- $^{66}\mathrm{C.}$ Sheppard and M. Gu, "Image formation in two-photon fluorescence microcopy," Optik $\mathbf{86}, 104\text{--}106 \, (1990).$
- ⁶⁷W. R. Zipfel, R. M. Williams, and W. W. Webb, "Nonlinear magic: Multiphoton microscopy in the biosciences," Nat. Biotechnol. **21**, 1369–1377 (2003).
- ⁶⁸ J. L. Chaloupka, Y. Fisher, T. J. Kessler, and D. D. Meyerhofer, "Single-beam, ponderomotive-optical trap for free electrons and neutral atoms," Opt. Lett. **22**, 1021–1023 (1997).
- ⁶⁹ J. Arlt and M. J. Padgett, "Generation of a beam with a dark focus surrounded by regions of higher intensity: The optical bottle beam," Opt. Lett. 25, 191–193 (2000).
- ⁷⁰T. A. Klar, S. Jakobs, M. Dyba, A. Egner, and S. W. Hell, "Fluorescence microscopy with diffraction resolution barrier broken by stimulated emission," Proc. Natl. Acad. Sci. U. S. A. 97, 8206–8210 (2000).
- ⁷¹B. Richards and E. Wolf, "Electromagnetic diffraction in optical systems, II. Structure of the image field in an aplanatic system," Proc. R. Soc. London, Ser. A 253, 358–379 (1959).
- ⁷² K. Y. Bliokh, F. J. Rodríguez-Fortuño, F. Nori, and A. V. Zayats, "Spin-orbit interactions of light," Nat. Photonics 9, 796–808 (2015).
- ⁷³B. Neupane, F. Chen, W. Sun, D. T. Chiu, and G. Wang, "Tuning donut profile for spatial resolution in stimulated emission depletion microscopy," Rev. Sci. Instrum. **84**, 043701 (2013).
- ⁷⁴Y. Zhao, J. S. Edgar, G. D. M. Jeffries, D. McGloin, and D. T. Chiu, "Spin-to-orbital angular momentum conversion in a strongly focused optical beam," Phys. Rev. Lett. **99**, 073901 (2007).
- ⁷⁵M. Vitek and I. Muševič, "Nanosecond control and optical pulse shaping by stimulated emission depletion in a liquid crystal," Opt. Express 23, 16921 (2015).